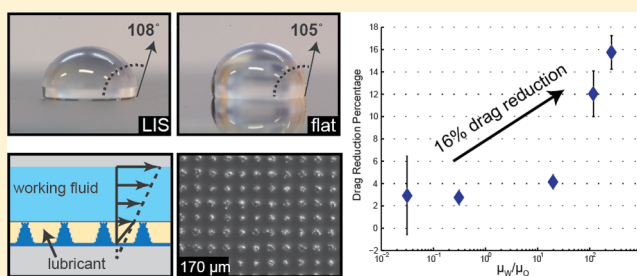


Drag Reduction using Lubricant-Impregnated Surfaces in Viscous Laminar Flow

Brian R. Solomon, Karim S. Khalil, and Kripa K. Varanasi*

Department of Mechanical Engineering, Massachusetts Institute of Technology, 77 Massachusetts Avenue, Cambridge, Massachusetts 02139, United States

ABSTRACT: Lubricant-impregnated surfaces (LIS), where micro/nanotextured surfaces are impregnated with lubricating liquids, have received significant attention for their robust, superslippy properties. In this study, we systematically demonstrate the potential for LIS to reduce drag in laminar flows. We present a scaling model that incorporates the viscosity of the lubricant and elucidates the dependence of drag reduction on the ratio of the viscosity of the working fluid to that of the lubricant. We experimentally validate this dependence in a cone and plate rheometer and demonstrate a drag reduction of 16% and slip length of 18 μm in the case where the ratio of working fluid viscosity to lubricant viscosity is 260.



INTRODUCTION

Surface modifications that reduce drag in fluid flows would benefit a multitude of industries. For example, maritime shipping is the world's most carbon-efficient form of transporting goods, yet it still accounts for 10% of global carbon emissions produced in transportation.¹ The reduction of the drag on ship hulls would benefit the environment and provide cost savings. Additionally, the United States has over two million kilometers of pipelines for transporting oil and natural gas that would also benefit from such a technology.²

To date, the most successful method of drag reduction in internal flows is the use of polymers in turbulent flows. The addition of only 10 parts per million of certain polymers is sufficient to produce drag reductions of up to 80% and is used in the oil industry, fire fighting equipment, irrigation, and sewage transport.^{3–5} Such additives work only in turbulent flow, and, furthermore, they must be continuously supplied. Alternatively, superhydrophobic surfaces that rely on trapped air pockets have been explored as a passive method of drag reduction.

Another application is microfluidics, where superhydrophobic grooves,^{6–9} carbon nanotubes,^{10,11} nanoscale spikes,¹² pillars,^{8,13} and meshes¹⁴ have been shown experimentally to reduce drag in laminar internal flows and in some cases produce slip lengths on the order of hundreds of microns.^{8,13,14} Superhydrophobic surfaces, however, lack robustness because air pockets can collapse and thus have limited practical applicability in the case of drag reduction.¹⁵ Surface defects, air dissolution,¹⁶ external forces, and phase transitions such as condensation and desublimation¹⁷ cause the desirable Cassie state to transition to a Wenzel state¹⁸ and erase any potential drag reduction benefits. Moreover, surfaces that rely on trapped air pockets and repel low-surface tension liquids require intricate surface textures.¹⁹

Whereas a superhydrophobic surface is a composite surface composed of a solid and air, a lubricant-impregnated surface (LIS) is composed of a solid and liquid lubricant. Lubricant-

impregnated surfaces have recently been shown to display low contact angle hysteresis,^{20–27} to be self-cleaning,^{23,28,29} and to promote dropwise condensation,^{30–32} anti-icing,^{33–36} and antifouling.^{37–41} These robust, slippy composite surfaces have great potential for drag reduction, but, to date, there have been no studies investigating drag reduction by LIS.

A droplet on an LIS can exist in several thermodynamically stable states that are dependent on the relative spreading coefficients of the lubricant and the droplet as well as the surface texture.²⁴ If an excess film is present that submerges the surface texture will eventually drain to reach these thermodynamically stable states, and any slippy properties attributed to these films^{21,28,33,27} will be compromised. A lubricant will spontaneously impregnate a texture given its contact angle on a chemically identical smooth surface is below a critical contact angle. The lubricant will impregnate a textured surface in vapor/air if $\theta_{os(v)} \leq \theta_c$, where $\theta_{os(v)}$ is the contact angle of lubricant (subscript o) on the smooth solid (subscript s) in the presence of vapor/air (subscript v) and θ_c is the critical contact angle for impregnation given by^{20,24}

$$\theta_c = \cos^{-1}[(1 - \phi_s)/(r - \phi_s)] \quad (1)$$

Here, ϕ_s is the fraction of the projected area of the textured surface that is occupied by a solid (the solid fraction) and r is the ratio of total surface area of the textured surface to its projected area. Analogously, the impregnation criterion for a surface under water is $\theta_{os(w)} \leq \theta_c$, where $\theta_{os(w)}$ is the contact angle of lubricant on the smooth solid in the presence of water (subscript w).

For these experiments, a surface must be chosen that can be textured and easily chemically functionalized to alter its surface

Received: June 3, 2014

Revised: August 13, 2014

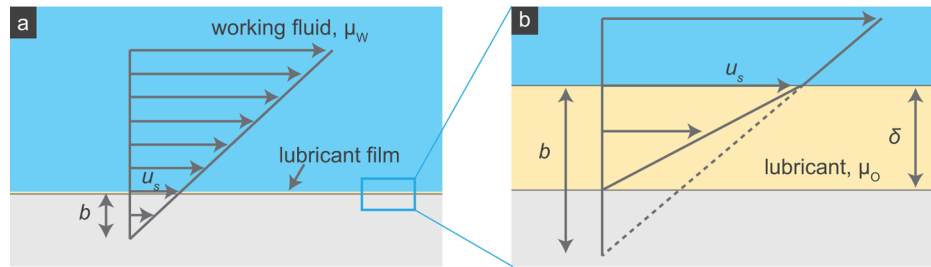


Figure 1. (a) Model for a working fluid flowing over a surface. (b) Details of the velocity profile for the hypothetical case of zero solid fraction in which the lubricant viscosity μ_o is less than the working fluid viscosity μ_w and results in an apparent slip length b .

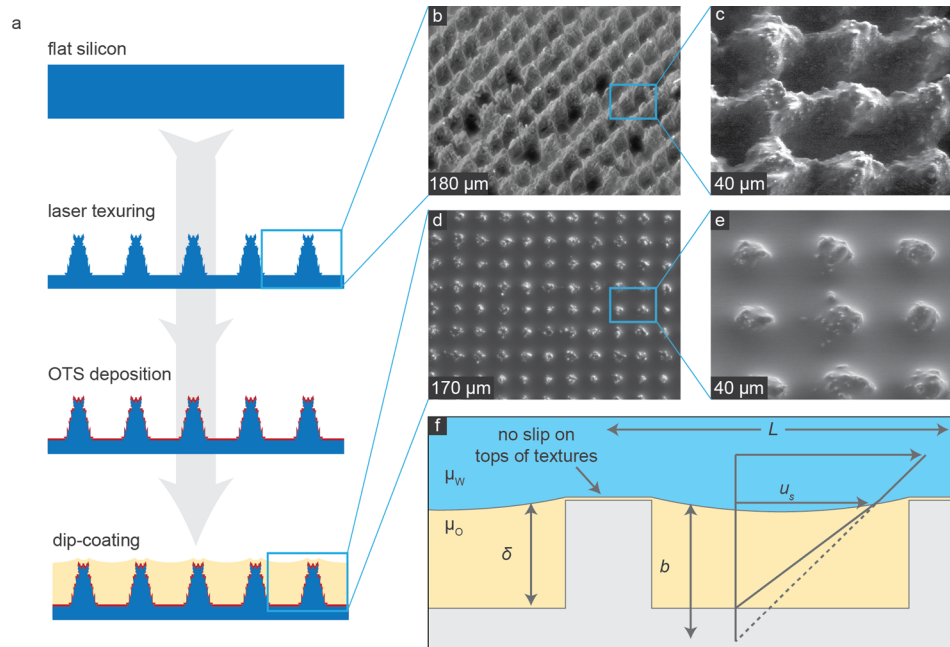


Figure 2. (a) Schematic showing the process to create the LIS surface used in this study. (b, c) SEM images of the laser textured surface showing both microscale and nanoscale features. (d, e) ESEM images of the LIS showing the oil lubricant completely filling the texture and protrusion of the tips of the texture. (f) Details of the velocity profile for a liquid-impregnated surface showing a local slip length b .

energy. Silicon wafers are readily available and are often functionalized with silane chemistries. A lubricant must be chosen that spontaneously impregnates the texture in air. Furthermore, the lubricant should also impregnate in the presence of water and glycerol which are used as working fluids in these experiments. Silicone oil readily spreads on flat silicon functionalized with octadecyltrichlorosilane (OTS) both in air ($\theta_{\text{os(v)}} = 0^\circ$) and in the presence of water. In addition, because the contact angle of silicone oil on the smooth solid in the presence of either water or glycerol is zero ($\theta_{\text{os(w)}} = 0^\circ$), silicone oil will fully spread over the textures beneath the working fluid and lead to virtually no droplet pinning. Thereby, silicon functionalized with OTS and silicone oil are chosen to form the LIS. A water droplet on this surface has an advancing contact angle of 108° , extremely low contact angle hysteresis ($<1^\circ$), and high droplet mobility and thus anticipates potential drag reduction.

Theoretically, maximum drag reduction is achieved in the case where the solid fraction ϕ_s of the texture is zero, as depicted in Figure 1b. Consider the laminar pressure driven flow of a working fluid of viscosity μ_w through a pipe of radius R with a layer of lubricant of viscosity μ_o and thickness δ separating the working fluid from the pipe wall. For a given flow rate, the drag reduction DR is taken to be one minus the ratio of the pressure drop required to pump the working fluid ΔP to the case without a

lubricant layer ΔP_0 . By matching the velocity and shear stress at the working fluid/lubricant interface and assuming that the thickness of the lubricating layer is sufficiently small ($\delta \ll R$), the drag reduction DR can be solved analytically as

$$(1 - DR)^{-1} = \frac{\Delta P_0}{\Delta P} = 1 + \frac{4\delta}{R} \left(\frac{\mu_w}{\mu_o} - 1 \right) - \frac{2\delta^2}{R^2} \left(\frac{2\mu_w}{\mu_o} - 1 \right) \quad (2)$$

In the above derivation, it is assumed that the velocity profile is quadratic in the working fluid and approximately linear in the lubricating layer. Note that to first order $DR \sim \mu_w/\mu_o$. Thus, it is only beneficial to use a lubricant that is less viscous than the working fluid, and more viscous working fluids experience greater drag reduction.

In order to demonstrate drag reduction by LIS and confirm the dependence on μ_w/μ_o , we fabricate LIS samples and compare them to flat samples using a cone and plate rheometer. We study systematically this dependence while taking steps to overcome the typical errors associated with rheometry.

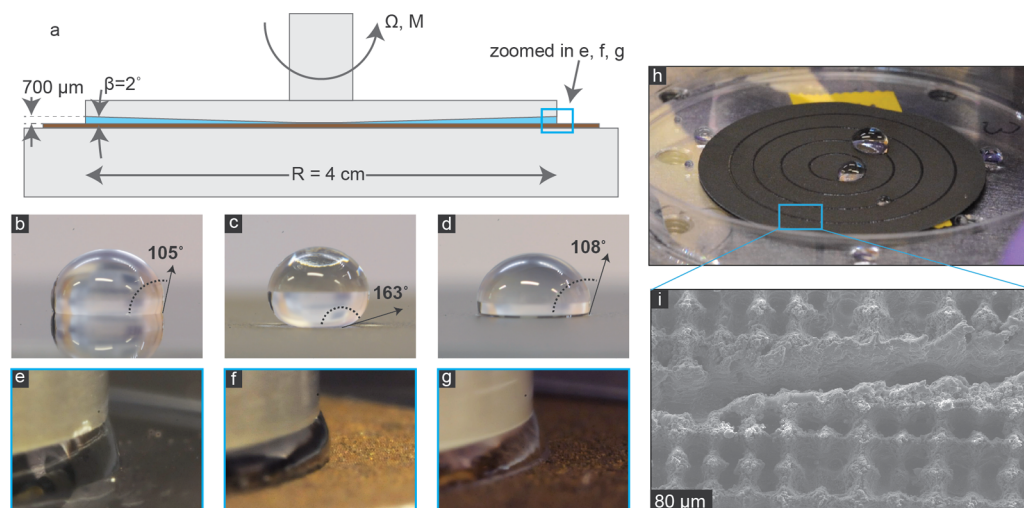


Figure 3. (a) Schematic of the cone and plate rheometer setup. (b–d) Images of a water droplet resting on a flat OTS-coated silicon wafer, superhydrophobic surface, and LIS, respectively. The inset numbers are static contact angles. (e–g) Images of the free surface of the working fluid between the cone and substrate for a flat OTS-coated silicon wafer, superhydrophobic surface, and LIS, respectively. Despite having drastically different contact angles, the free surfaces are identical. (h) A laser ablated circle pins water droplets on an otherwise superhydrophobic surface. (i) SEM image of the laser ablated circle.

EXPERIMENTAL METHODS

Surface Fabrication. To construct an LIS, it is necessary that the lubricant be immiscible with the working fluid and that the system is thermodynamically stable.²⁴ When a water droplet is placed on an LIS surface, we refer to the portion of the solid covered with a thin layer of lubricant in contact with the working fluid as the tops of the texture. The resulting surface behaves as depicted in Figure 2f, where the lubricant is held in the textures and the working fluid flows above it. For this study, we chose water–glycerol mixtures as the working fluid and oils of varying viscosities as the lubricant. This allows us to span several orders of magnitude in the viscosity ratio μ_w/μ_o .

Figure 2a shows a schematic of the sample preparation method. As received 2" diameter polished silicon wafers (University Wafer) are subjected to a laser ablation process. A 1064 nm Nd:YAG laser (Electrox) is rastered across the surface in a controlled pattern.⁴² The resulting texture is well-ordered and reproducible with postlike features spaced approximately 50 μm apart and 50 μm deep that are covered with nanoscale features (Figure 2b,c). The wafers are then coated with a hydrophobic monomer octadecyltrichlorosilane (OTS, Sigma-Aldrich). A circle approximately 20 mm in radius is then laser ablated from the coated sample (seen in Figure 3h,i). This step ablates hydrophobic material to reveal the underlying hydrophilic silicon. The utility of this step in pinning the free surface of the working fluid is described later.

Finally, samples are dip-coated in lubricant oils to create LIS. To create a thermodynamically stable film, the dip coating withdrawal velocity must be below a critical speed $V_{\text{crit}} = 0.121\mu_o\gamma(\delta/l_c)^{3/2}$, where μ_o is the viscosity of the lubricant, γ is its surface tension, l_c is its capillary length, and δ is the depth of the texture.⁴³ Accordingly, samples are dip-coated at a maximum withdrawal speed of 1 mm/s. Flat control samples are coated with OTS, and then a 20 mm circle is ablated in similar fashion, but flat control samples did not undergo the first laser texturing step or subsequent dip coating.

An environmental scanning microscope (Philips XL30 FEG ESEM) is used to image the final LIS. A typical image is taken at an accelerating voltage of 10 kV at a pressure of 100 Pa. Figure 2e reveals lubricant inside the textures while the tops of the textures are visible. Although not visible, a thin lubricant film spreads over the tops of the textures.²⁴

A water droplet on the flat silicon samples coated with OTS has advancing and receding contact angles of 110 and 98°, respectively (Figure 3b). Prior to impregnation of the lubricant, the surface is superhydrophobic and has an advancing and receding contact angle of 164 and 162° (Figure 3c). The LIS has an advancing contact angle of $108 \pm 2^\circ$ and a receding contact angle $107 \pm 2^\circ$ (Figure 3d). Although

these are considerably lower angles than that of the superhydrophobic surface, its contact angle hysteresis was extremely low ($<1^\circ$). Cassie–Baxter theory relates the contact angle on a superhydrophobic surface to that on a chemically identical smooth surface by $\cos \theta_{\text{SHo}} = \phi_s(\theta_{\text{flat}} - 1) + 1$.⁴⁴ Taking the static contact angles $\theta_{\text{SHo}} = 163^\circ$ and $\theta_{\text{flat}} = 105^\circ$ (shown in Figure 3) gives the solid fraction $\phi_s \approx 0.06$. Alternatively, the solid fraction can be estimated as the area of visible solid in SEM micrographs (Figure 3e) per unit area to yield $\phi_s \approx 0.08$.

Rheometry. To probe the drag reduction capabilities of LIS, a rheometer (AR-G2, TA Instruments) is used. A cone and plate geometry (depicted in Figure 3a) with a 40 mm diameter cone (2° , 1' cone angle, 54 μm truncation gap) is used. Because, generally, a fluid becomes less viscous at higher temperatures, a fluid undergoing shear heating in this setup would incorrectly imply higher drag reduction. The degree of shear heating is characterized by the Brinkman number, which, for this flow geometry, is $Br = \mu_w R^2 \Omega^2 / (kT)$, where μ_w is the viscosity of the working fluid, R is the cone radius, Ω is the angular velocity, k is the working fluid's thermal conductivity, and T is its temperature. The deviation in torque is roughly $b_0 Br / 12$, where b_0 characterizes the dependence of viscosity on temperature⁴⁵ (roughly 0.1 for glycerol solutions). With the most viscous working fluid at the highest shear rates, it is estimated that the torque will deviate by less than 0.4% as a result of shear heating. Conversely, inertial effects would tend to increase dissipation and thus would imply higher drag. The characteristic Reynolds number is $Re = \rho \Omega \beta^2 R^2 / \mu_w$, where β is the cone angle and is low for all experiments. In trial experiments at very high shear rates, the measured viscosity for Newtonian fluid samples is lower as compared to that at lower shear rates. This suggests that shear heating effects influence the data before inertial effects do.

At low shear rates, noise associated with ambient vibration is dominant. Accordingly, the shear rate $\dot{\gamma} = \Omega/\beta$ is kept in the range of 10–100 s^{-1} to avoid noise on the low end and shear heating on the high end. All samples are tested on a Peltier stage controlled to 25 °C.

For varying the viscosity ratio, pure glycerol (Sigma-Aldrich) is diluted with 18 M Ω deionized water (Millipore) and used as a working fluid. The lubricant oil is either 10 or 100 cSt silicone oil (Sigma-Aldrich). In addition, viscosity standard N1000 calibration fluid (Cannon Instrument Company) is used as a working fluid as received. Its viscosity is significantly greater than that of pure glycerol.

Over the course of an experiment, water can absorb/desorb from the working fluid. Separate experiments measuring the absorption/desorption of water from glycerol–water solutions show the weight change to be less than 0.5%.

Each experiment is conducted at least three times. Between experiments, the working fluid is replaced, and the sample is realigned. The truncation gap is also reset, and standard calibration on the rheometer is performed. A typical experiment lasts 15 min.

Pinning of the Free Surface. Edge effects are the largest source of error in rheometry experiments.^{46,47} In calculations in this article, it is assumed that the free surface is a spherical cap and that a consistent velocity field is maintained up to the boundary. Careful precautions are taken to ensure this.

Owing to different wettability of the control surfaces compared to that of LIS, a significant difference in measured torques would arise if this discrepancy is not controlled.⁴⁸ As depicted in Figure 3b–d, a substrate with a higher contact angle has less working fluid in contact with it. As a result, the measured torque will be lower and result erroneously in measured drag reduction. To control this, we introduce a hydrophilic pinning line to force the contact line of the working fluid to be reproducible across all samples. The volume of working fluid is controlled by a precision micropipette (BrandTech Scientific). The shape of the free surface is monitored by camera. For each experiment, the shape of the free surface is visually matched to a reference image to ensure that the edge condition is consistent. The surfaces of Figure 3b–d all produce the same free surface when pinning lines are present as shown in Figure 3e–g.

After loading the working fluid onto the substrate, the cone is lowered to the truncation gap height. Because LIS exhibit such low contact angle hysteresis and are extremely slippery, working fluid is easily pushed out from the cone and outer pinning ring even when the cone is slowly lowered. As a result, we introduce four concentric pinning circles to each sample to control the spreading of working fluid as the cone is lowered. These pinning circles are also used with the flat control samples for consistency. The pinning circles occupy less than 0.6% of the surface area and do not significantly impact measurements.

RESULTS AND DISCUSSION

A convenient way to model drag reduction is to introduce the apparent slip length. Contrary to the traditional no-slip condition, the Navier slip condition posits a velocity u_s at the boundary interface proportional to the shear stress τ_{yx} at the interface by the slip length b (Figure 1a).

$$u_s = \frac{b}{\mu} \tau_{yx} \Big|_{\text{interface}} \quad (3)$$

Thus, the slip velocity and slip length are inherently taken to be area-averaged quantities because the slip velocity varies spatially on the boundary. For example it is smallest at the tops of texture features.

On a superhydrophobic surface, stress-free interfaces between the working fluid and the trapped air within the composite solid results in an apparent slip length.⁴⁹ For postlike arrays, this slip length can be described by $b_{\tau=0}/L = A/(\phi_s)^{1/2} - B$, where the constants A and B have been deduced computationally and analytically.^{50–52} As the trapped fluid's viscosity increases, its contribution to shear is increasingly more relevant. A heuristic formula incorporating viscous dissipation within the trapped air or lubricant is⁵⁰

$$\frac{1}{b} = \frac{\mu_o q}{(1 - \phi_s) \mu_w \tanh q \delta} + \frac{1}{b_{\tau=0}} \quad (4)$$

where δ is the thickness of the lubricant and q describes the hydrodynamic interactions between postlike structures.^{50,53} Clearly, for negligible lubricant viscosity μ_o , the shear-free case is recovered in which the slip length b is independent of the viscosity ratio μ_w/μ_o . At some point, the slip length becomes dependent on μ_w/μ_o and in general depends on the lubricant viscosity, periodicity, texture geometry, solid fraction, and

thickness of the lubricant. By simplification of eq 4 in this viscosity-dependent regime, the slip length scales as

$$b \sim \frac{\mu_w}{\mu_o} (1 - \phi_s) \delta \quad (5)$$

Assuming a no-slip boundary condition and laminar flow, the apparent viscosity measured for a given configuration and working fluid is $\mu_{w,\text{app}} = 3\beta M / (2\pi\Omega R^3)$.⁴⁵ For an LIS that reduces drag, the ratio of apparent viscosity to actual viscosity $\mu_{w,\text{app}}/\mu_w$ is less than 1. An experimental plot of this ratio $\mu_{w,\text{app}}/\mu_w$ versus the ratio of working fluid to lubricant viscosity μ_w/μ_o is shown in Figure 4a. Consistent with the aforementioned theory, drag reduction is greater for more viscous working fluids.

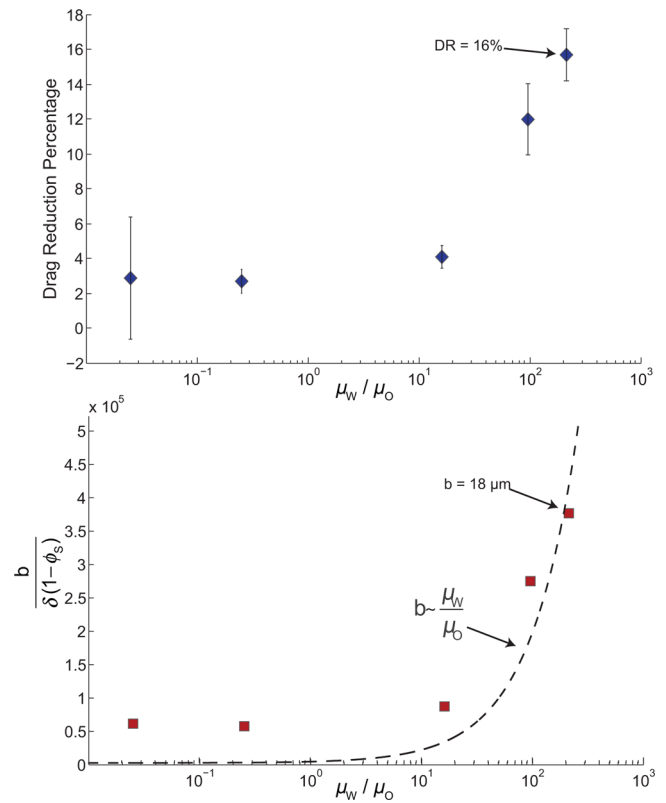


Figure 4. (a) Plot of the drag reduction percentage vs the ratio of the working fluid to lubricant viscosity. (b) Plot of the computed apparent averaged slip length vs the ratio of the working fluid to lubricant viscosity.

It is instructive to extract a space-averaged apparent slip length from the torque measurements in order to extend these results to practical flows (like the pipe flow solved by eq 2). Solving the Navier–Stokes equations in spherical coordinates and applying the Navier slip boundary condition gives the relationship between the measured torque M and the average slip length b as⁸

$$M = \frac{2\pi \mu_w \Omega R^3}{3\beta} \left(1 - \frac{3b}{2R\beta} + \frac{3b^2}{R^2\beta^2} \right) - 2\pi\Omega\mu_w \frac{b^3}{\beta^4} \ln \left(\frac{R\beta + b}{b} \right) \quad (6)$$

This equation is numerically solved for the slip length. The results are presented in Figure 4b alongside the expected scaling of eq 5.

Table 1. Measured Drag Reduction and Slip Lengths for Varying Working Fluid to Lubricant Viscosity Ratios

working fluid viscosity μ_w (cP)	lubricant viscosity μ_o (cP)	viscosity ratio μ_w/μ_o	characteristic torque (mN m)	drag reduction DR%	slip length b (μm)
2.4	76	0.031	0.1	2.9	2.7
2.4	7.6	0.31	0.1	2.7	2.1
150.4	7.6	20	7	4.1	4.1
894.2	7.6	118	43	12	13.1
1985	7.6	261	95	16	18

Table 2. Comparison of Drag Reduction and Slip Lengths Reported in the Literature

flow geometry	surface	viscosity ratio μ_w/μ_o	solid fraction ϕ_s	periodicity L (μm)	drag reduction DR%	slip length b (μm)	b/L
microchannel ¹⁰	carbon nanotube forest	45	0.1	6		1.5	0.25
cone-plate ¹² rheometer	silicon needles	40		0.5–1		50	
16 mm diameter pipe ⁵⁴	acrylic resin	45			14		0.25
microchannel ⁶	microridges	45	0.2	100	40	24	1
channel (turbulent) ⁵⁵	microridges	45	0.5	120	50	120	0.925
cone-plate rheometer ⁸	concentric microridges	45	0.02	200		185	
cone-plate rheometer ¹³	concentric microridges	45	0.02	450 ^a		400	0.889
microchannel ⁷	microridges	45	0.5	30	25		
12 mm cylinder in water tunnel ⁵⁶	hydrophobized sand	45			28		0.101
Couette cell ⁹	microridges		0.5	50	20		
parallel-plate rheometer ¹⁴	spray-coated mesh	310	0.41	2100/32 ^a		213	0.36
cone-plate rheometer	laser ablated posts (this work)	261	0.06	50	16	18	

^aSurface comprised a dual-scale texture.

For working fluids with a viscosity around that of the lubricant ($\mu_w < 30\mu_o$), little or no drag reduction is observed. Experiments at the highest value of μ_w/μ_o have characteristic torques three magnitudes greater than those at the lowest (Table 1). We observe that measurements at low μ_w/μ_o are thus less sensitive, which explains the slight drag reduction seen for the lowest viscosity ratios. As the working fluid becomes more viscous ($\mu_w > 100\mu_o$), drag reduction is observed. With the most viscous working fluid ($\mu_w = 210\mu_o$), a drag reduction of 16% is observed, which correlates to a slip length of 18 μm .

Table 2 presents the reported slip lengths of other researchers and this study along with relevant parameters where available. Note that b/L is roughly consistent, indicating that in these experiments the effect of viscous dissipation in trapped air or lubricant is negligible. As shown in our experiment (Figure 4) at lower viscosity ratios, viscous dissipation within the lubricant is important. For a given surface, the regime in which the viscosity ratio affects the slip length is dependent on the parameters of the texture following from eq 4.

To date, the highest slip length of 400 μm has been achieved on a superhydrophobic surface (essentially an LIS with air as a lubricant) by designing robust, high periodicity structures with low solid fraction.¹³ In this case, the working fluid to lubricant viscosity ratio is 45. One would expect a high slip length could be achieved for an LIS by designing a similar texture and impregnating it with a lubricant.

These results demonstrate that, similar to superhydrophobic surfaces, LIS reduce drag in laminar internal flows but have the additional advantage of increased pressure stability. Consistent with eq 2, significant drag reduction in pipe flow is expected only when the diameter of the pipe is of the order of the slip length. Accordingly, drag reduction using LIS shows immediate promise for application in microfluidics. These results prompt similar studies for turbulent flows in which we theorize drag reduction can be achieved by effecting the dynamics of the viscous

sublayer.⁵⁷ In addition to future studies in the turbulent regime, the dependence on solid fraction should also be confirmed.

Modifying the structure and periodicity of the texture can optimize LIS for drag reduction. For example, grooves that are longitudinal to the flow should offer better drag reduction than those transverse, as shown analogously for superhydrophobic surfaces.^{58,59} Although LIS show promise for drag reduction, the lubricant can deplete over time due to its solubility in the working fluid³⁰ and can also drain over time. A lubricant reservoir to replenish the lubricant can overcome these issues.

CONCLUSIONS

We systematically demonstrate drag reduction using LIS for a variety of lubricant to working fluid viscosity ratios using cone and plate rheometry. The free surface of the working fluid in the rheometer is carefully controlled to prevent error. Consistent with theory, we find the drag reduction is highest for the most viscous working fluid ($\mu_w = 260\mu_o$), and its measured slip length is 18 μm . Performance can be improved by optimizing the texture design and longevity issues associated with solubility, and drainage can be overcome by designing a replenishing lubricant reservoir.

AUTHOR INFORMATION

Corresponding Author

*E-mail: varanasi@mit.edu. Phone: 617-324-5608.

Notes

The authors declare no competing financial interest.

ACKNOWLEDGMENTS

We gratefully acknowledge the support of Shell-MIT Energy Initiative. B.R.S. acknowledges support from the MITEI Fellowship. We thank Professor Gareth McKinley for use of

the Hatsopoulos Microfluids Laboratory and Professor Tonio Buonassisi for use of the laser cutter.

REFERENCES

- (1) Buhaug, Ø.; Corbett, J. J.; Endresen, O.; Eyring, V.; Faber, J.; Hanayama, S.; Lee, D.; Lindstad, H.; Mjelde, A.; Palsson, C. *Second International Maritime Organization Green House Gases Study 2009*; International Maritime Organization: London, 2009.
- (2) *The World Factbook 2013–14*; Central Intelligence Agency: Washington, DC, 2013.
- (3) Lumley, J. L. Drag Reduction by Additives. *Annu. Rev. Fluid Mech.* **1969**, *1*, 367–384.
- (4) Berman, N. S. Drag Reduction by Polymers. *Annu. Rev. Fluid Mech.* **1978**, *10*, 47–64.
- (5) Sellin, R. H. J.; Ollis, M. Polymer Drag Reduction in Large Pipes and Sewers: Results of Recent Field Trials. *J. Rheol.* **1980**, *24*, 667–684.
- (6) Ou, J.; Perot, B.; Rothstein, J. P. Laminar Drag Reduction in Microchannels Using Ultrahydrophobic Surfaces. *Phys. Fluids* **2004**, *16*, 4635–4643.
- (7) Ou, J.; Rothstein, J. P. Direct Velocity Measurements of the Flow Past Drag-Reducing Ultrahydrophobic Surfaces. *Phys. Fluids* **2005**, *17*, 103606.
- (8) Lee, C.; Choi, C.-H.; Kim, C.-J. Structured Surfaces for a Giant Liquid Slip. *Phys. Rev. Lett.* **2008**, *101*, 064501.
- (9) Truesdell, R.; Mammoli, A.; Vorobieff, P.; van Swol, F.; Brinker, C. J. Drag Reduction on a Patterned Superhydrophobic Surface. *Phys. Rev. Lett.* **2006**, *97*, 044504.
- (10) Joseph, P.; Cottin-Bizonne, C.; Benoit, J.-M.; Ybert, C.; Journet, C.; Tabeling, P.; Bocquet, L. Slippage of Water Past Superhydrophobic Carbon Nanotube Forests in Microchannels. *Phys. Rev. Lett.* **2006**, *97*, 156104.
- (11) Ming, Z.; Jian, L.; Chunxia, W.; Xiaokang, Z.; Lan, C. Fluid Drag Reduction on Superhydrophobic Surfaces Coated with Carbon Nanotube Forests (CNTs). *Soft Matter* **2011**, *7*, 4391–4396.
- (12) Choi, C.-H.; Kim, C.-J. Large Slip of Aqueous Liquid Flow over a Nanoengineered Superhydrophobic Surface. *Phys. Rev. Lett.* **2006**, *96*, 066001.
- (13) Lee, C.; Kim, C.-J. Maximizing the Giant Liquid Slip on Superhydrophobic Microstructures by Nanostructuring Their Sidewalls. *Langmuir* **2009**, *25*, 12812–12818.
- (14) Srinivasan, S.; Choi, W.; Park, K.-C.; Chhatre, S. S.; Cohen, R. E.; McKinley, G. H. Drag Reduction for Viscous Laminar Flow on Spray-Coated Non-Wetting Surfaces. *Soft Matter* **2013**, *9*, 5691–5702.
- (15) Bocquet, L.; Lauga, E. A Smooth Future? *Nat. Mater.* **2011**, *10*, 334–337.
- (16) Patankar, N. A. Vapor Stabilizing Substrates for Superhydrophobicity and Superslip. *Langmuir* **2010**, *26*, 8783–8786.
- (17) Varanasi, K. K.; Deng, T.; Smith, J. D.; Hsu, M.; Bhate, N. Frost Formation and Ice Adhesion on Superhydrophobic Surfaces. *Appl. Phys. Lett.* **2010**, *97*, 234102.
- (18) Deng, T.; Varanasi, K. K.; Hsu, M.; Bhate, N.; Keimel, C.; Stein, J.; Blohm, M. Nonwetting of Impinging Droplets on Textured Surfaces. *Appl. Phys. Lett.* **2009**, *94*.
- (19) Tuteja, A.; Choi, W.; Ma, M.; Mabry, J. M.; Mazzella, S. A.; Rutledge, G. C.; McKinley, G. H.; Cohen, R. E. Designing Superoleophobic Surfaces. *Science* **2007**, *318*, 1618–1622.
- (20) Quéré, D. Non-Sticking Drops. *Rep. Prog. Phys.* **2005**, *68*, 2495.
- (21) Wong, T.-S.; Kang, S. H.; Tang, S. K. Y.; Smythe, E. J.; Hatton, B. D.; Grinthal, A.; Aizenberg, J. Bioinspired Self-Repairing Slippery Surfaces with Pressure-Stable Omniphobicity. *Nature* **2011**, *477*, 443–447.
- (22) Nishimoto, S.; Bhushan, B. Bioinspired Self-Cleaning Surfaces with Superhydrophobicity, Superoleophobicity, and Superhydrophilicity. *RSC Adv.* **2013**, *3*, 671–690.
- (23) Lafuma, A.; Quéré, D. Slippery Pre-Suffused Surfaces. *Europhys. Lett.* **2011**, *96*, 56001.
- (24) Smith, J. D.; Dhiman, R.; Anand, S.; Reza-Garduno, E.; Cohen, R. E.; McKinley, G. H.; Varanasi, K. K. Droplet Mobility on Lubricant-Impregnated Surfaces. *Soft Matter* **2013**, *9*, 1772–1780.
- (25) Huang, X.; Chrisman, J. D.; Zacharia, N. S. Omniphobic Slippery Coatings Based on Lubricant-Infused Porous Polyelectrolyte Multilayers. *ACS Macro Lett.* **2013**, *2*, 826–829.
- (26) Carlson, A.; Kim, P.; Amberg, G.; Stone, H. A. Short and Long Time Drop Dynamics on Lubricated Substrates. *Europhys. Lett.* **2013**, *104*, 34008.
- (27) Eifert, A.; Paulssen, D.; Varanakkottu, S. N.; Baier, T.; Hardt, S. Simple Fabrication of Robust Water-Repellent Surfaces with Low Contact-Angle Hysteresis Based on Impregnation. *Adv. Mater. Interfaces* **2014**, DOI: 10.1002/admi.201300138.
- (28) Yao, X.; Hu, Y.; Grinthal, A.; Wong, T.-S.; Mahadevan, L.; Aizenberg, J. Adaptive Fluid-Infused Porous Films with Tunable Transparency and Wettability. *Nat. Mater.* **2013**, *12*, 529–534.
- (29) Liu, H.; Zhang, P.; Liu, M.; Wang, S.; Jiang, L. Organogel-Based Thin Films for Self-Cleaning on Various Surfaces. *Adv. Mater.* **2013**, *25*, 4477–4481.
- (30) Anand, S.; Paxson, A. T.; Dhiman, R.; Smith, J. D.; Varanasi, K. K. Enhanced Condensation on Lubricant-Impregnated Nanotextured Surfaces. *ACS Nano* **2012**, *6*, 10122–10129.
- (31) Xiao, R.; Miljkovic, N.; Enright, R.; Wang, E. N. Immersion Condensation on Oil-Infused Heterogeneous Surfaces for Enhanced Heat Transfer. *Sci. Rep.* **2013**, *3*.
- (32) Rykaczewski, K.; Paxson, A. T.; Staymates, M.; Walker, M. L.; Sun, X.; Anand, S.; Srinivasan, S.; McKinley, G. H.; Chinn, J.; Scott, J. H. J.; et al. Dropwise Condensation of Low Surface Tension Fluids on Omniphobic Surfaces. *Sci. Rep.* **2014**, *4*.
- (33) Kim, P.; Wong, T.-S.; Alvarenga, J.; Kreder, M. J.; Adorno-Martinez, W. E.; Aizenberg, J. Liquid-Infused Nanostructured Surfaces with Extreme Anti-Ice and Anti-Frost Performance. *ACS Nano* **2012**, *6*, 6569–6577.
- (34) Vogel, N.; Belisle, R. A.; Hatton, B.; Wong, T.-S.; Aizenberg, J. Transparency and Damage Tolerance of Patternable Omniphobic Lubricated Surfaces Based on Inverse Colloidal Monolayers. *Nat. Commun.* **2013**, *4*, 2176.
- (35) Subramanyam, S. B.; Rykaczewski, K.; Varanasi, K. K. Ice Adhesion on Lubricant-Impregnated Textured Surfaces. *Langmuir* **2013**, *29*, 13414–13418.
- (36) Chen, L.; Geissler, A.; Bonaccorso, E.; Zhang, K. Transparent Slippery Surfaces Made with Sustainable Porous Cellulose Lauroyl Ester Films. *ACS Appl. Mater. Interfaces* **2014**, *6*, 6969–6976.
- (37) Epstein, A. K.; Wong, T.-S.; Belisle, R. A.; Boggs, E. M.; Aizenberg, J. Liquid-Infused Structured Surfaces with Exceptional Anti-Biofouling Performance. *Proc. Natl. Acad. Sci. U.S.A.* **2012**, *109*, 13182–13187.
- (38) Ueda, E.; Levkin, P. A. Micropatterning Hydrophobic Liquid on a Porous Polymer Surface for Long-Term Selective Cell-Repellency. *Adv. Healthcare Mater.* **2013**, 1425–1429.
- (39) Li, J.; Kleintschek, T.; Rieder, A.; Cheng, Y.; Baumbach, T.; Obst, U.; Schwartz, T.; Levkin, P. A. Hydrophobic Liquid-Infused Porous Polymer Surfaces for Antibacterial Applications. *ACS Appl. Mater. Interfaces* **2013**, *5*, 6704–6711.
- (40) Xiao, L.; Li, J.; Mieszkina, S.; Di Fino, A.; Clare, A. S.; Callow, M. E.; Callow, J. A.; Grunze, M.; Rosenhahn, A.; Levkin, P. A. Slippery Liquid-Infused Porous Surfaces Showing Marine Antibiofouling Properties. *ACS Appl. Mater. Interfaces* **2013**, *5*, 10074–10080.
- (41) Subramanyam, S. B.; Azimi, G.; Varanasi, K. K. Designing Lubricant-Impregnated Textured Surfaces to Resist Scale Formation. *Adv. Mater. Interfaces* **2014**, 1300068.
- (42) Bird, J. C.; Dhiman, R.; Kwon, H.-M.; Varanasi, K. K. Reducing the Contact Time of a Bouncing Drop. *Nature* **2013**, *503*, 385–388.
- (43) Seiwert, J.; Clanet, C.; Quéré, D. Coating of a Textured Solid. *J. Fluid Mech.* **2011**, *669*, 55–63.
- (44) Cassie, A. B. D.; Baxter, S. Wettability of Porous Surfaces. *Trans. Faraday Soc.* **1944**, *40*, 546–551.
- (45) Macosko, C. W. *Rheology: Principles, Measurements, and Applications*; VCH: New York, 1994.
- (46) Bocquet, L.; Tabeling, P.; Manneville, S. Comment on “Large Slip of Aqueous Liquid Flow over a Nanoengineered Superhydrophobic Surface”. *Phys. Rev. Lett.* **2006**, *97*, 109601.

- (47) Choi, C.-H.; Kim, C.-J. Choi and Kim Reply. *Phys. Rev. Lett.* **2006**, *97*, 109602.
- (48) Johnston, M. T.; Ewoldt, R. H. Precision Rheometry: Surface Tension Effects on Low-Torque Measurements in Rotational Rheometers. *J. Rheol.* **2013**, *57*, 1515–1532.
- (49) Granick, S.; Zhu, Y.; Lee, H. Slippery Questions about Complex Fluids Flowing Past Solids. *Nat. Mater.* **2003**, *2*, 221–227.
- (50) Ybert, C.; Barentin, C.; Cottin-Bizonne, C.; Joseph, P.; Bocquet, L. Achieving Large Slip with Superhydrophobic Surfaces: Scaling Laws for Generic Geometries. *Phys. Fluids* **2007**, *19*, 123601.
- (51) Ng, C.-O.; Wang, C. Y. Apparent Slip Arising from Stokes Shear Flow over a Bidimensional Patterned Surface. *Microfluid. Nanofluid.* **2010**, *8*, 361–371.
- (52) Davis, A. M. J.; Lauga, E. Hydrodynamic Friction of Fakir-like Superhydrophobic Surfaces. *J. Fluid Mech.* **2010**, *661*, 402–411.
- (53) Sangani, A. S.; Acrivos, A. Slow Flow through a Periodic Array of Spheres. *Int. J. Multiphase Flow* **1982**, *8*, 343–360.
- (54) Watanabe, K.; Udagawa, Y.; Udagawa, H. Drag Reduction of Newtonian Fluid in a Circular Pipe with a Highly Water-Repellent Wall. *J. Fluid Mech.* **1999**, *381*, 225–238.
- (55) Daniello, R. J.; Waterhouse, N. E.; Rothstein, J. P. Drag Reduction in Turbulent Flows over Superhydrophobic Surfaces. *Phys. Fluids* **2009**, *21*, 085103.
- (56) Brennan, J. C.; Fairhurst, D. J.; Morris, R. H.; McHale, G.; Newton, M. I. Investigation of the Drag Reducing Effect of Hydrophobized Sand on Cylinders. *J. Phys. Appl. Phys.* **2014**, *47*, 205302.
- (57) Sirovich, L.; Karlsson, S. Turbulent Drag Reduction by Passive Mechanisms. *Nature* **1997**, *388*, 753–755.
- (58) Sbragaglia, M.; Prosperetti, A. A Note on the Effective Slip Properties for Microchannel Flows with Ultrahydrophobic Surfaces. *Phys. Fluids* **2007**, *19*, 043603.
- (59) Feuillebois, F.; Bazant, M. Z.; Vinogradova, O. I. Effective Slip over Superhydrophobic Surfaces in Thin Channels. *Phys. Rev. Lett.* **2009**, *102*, 026001.